Study of turbulence-induced refraction of Lower Hybrid waves using synthetic Scrape-off Layer filaments

Bodhi Biswas*, Seung Gyou Baek, Paul Bonoli, Syun'ichi Shiraiwa, Gregory Wallace, Anne White

Plasma Science and Fusion Center,
Massachusetts Institute of Technology

Dated: May 28, 2021

Abstract

Turbulence-induced refraction effects to Lower Hybrid (LH) wave propagation and current drive are studied using synthetic scrape-off layer (SOL) blob/filament fields. A synthetic 3D, field-following, blob turbulence model is implemented in the ray-tracing/Fokker-Planck (RTFP) codes GENRAY/CQL3D. In Alcator C-Mod, the blob field is shown to significantly affect LH ray-trajectories, leading to increased on-axis damping and smoother current profiles. This effect depends on the average blob size and amplitude. In addition, the diffusion of ray-trajectories in phase-space caused by turbulence increases the robustness of the RTFP model. A modified $N_{||}$ launch spectrum, acting as a proxy for parametric decay instability (PDI) effects, is included in simulations with the blob model. A synergy between the modified launch spectrum and turbulence-induced refraction results in synthetic hard X-ray (HXR) profiles that agree with experiment. Lastly, the blob model is used to predict the effect of SOL turbulence on DIII-D high-field side (HFS) LH launch. Assuming low turbulence amplitude in the HFS SOL ($\sim 5\%$), turbulence-induced refraction is predicted to have little effect on current drive efficiency.

1 Introduction

1.1 Motivation for studying LH wave propagation

Lower hybrid waves ($\omega_{ci}^2 \ll \omega^2 \ll \omega_{ce}^2$) are demonstrated to efficiently drive toroidal current in a tokamak. Here, ω_{ce} (ω_{ci}) is the electron (ion) cyclotron frequency. They are an attractive candidate to shape the off-axis steady-state current profile, generate internal transport barriers, and mitigate neoclassical tearing modes [1–3]. To ensure strong single-pass absorption, LH waves must satisfy two conditions [4]. First, waves must be accessible to the target damping region: $N_{||}^2 \gtrsim 1 + \omega_{pe_{targ}}^2/\omega_{ce_{targ}}^2$, where $N_{||} \equiv k_{||}c/\omega$ is the wave refractive index parallel to the background magnetic field B, and ω_{pe} is the electron plasma frequency. Second, $N_{||}$ must be high enough for the wave to Landau damp on a sufficiently large population of electrons. This requires: $N_{||}^2 \gtrsim 20/T_{e_{targ}}[keV]$. The highest possible launched $N_{||}$ is determined by engineering

*E-mail: bodhib@mit.edu; Corresponding author

constraints. The first condition can be met by operating at sufficiently low densities. The second condition proves problematic for present-day tokamaks with LHCD systems, (ex. Alcator C-Mod and EAST), where core T_e is too low. In such a scenario, LH waves must make multiple passes to completely damp. Consequenty, they may be significantly affected by RF-edge interactions like collisional loss [5, 6], turbulent scattering [7–10], and parametric decay instabilities [11–13]. Standard ray-tracing/Fokker-Plack (RTFP) models of LHCD, which only account for core interactions, have difficulty matching experimental profiles for hard X-ray (HXR) count and toroidal current (J_{tor}). In C-Mod, the measured J_{tor} profile is robustly peaked on-axis and monotonically decreasing [14]. Meanwhile, RTFP modeling predicts predominantly off-axis current drive. Similarly, in Tore Supra, there exists a discrepancy in measured HXR profile and the predicted electron Landau damping (ELD) power deposition profile [15]. In both cases, radial diffusion of fast electrons is insufficient to bridge this discrepancy. This discrepancy is commonly called the "spectral-gap" in the LH community, and it may, in part, be explained by RF-edge interactions.

RTFP results are also found to be quite sensitive to core profiles, magnetic equilibrium, and initial LH launch conditions when in the multi-pass regime [14, 16]. In contrast, measured HXR profiles in C-Mod are remarkably robust across discharges with varying $\overline{n_e}$ and launched $N_{||}$ [14]. This suggests that RF-edge interactions may broaden the LH wave-number spectrum, effectively diffusing the ray trajectories in phase-space when they are otherwise sensitive to initial conditions. In addition, RF-edge interactions may increase first-pass damping in an otherwise multi-pass scenario, which further increases robustness of RTFP models.

The issue of deleterious RF-edge interactions motivate the launch of LH waves from the high-field side (HFS) in DIII-D [17]. First, the HFS SOL is relatively quiescent [18,19]. Second, HFS launch in DIII-D is expected to increase wave accessibility and result in strong single-pass damping for high temperature discharges. Both factors mitigate the influence of RF-turbulence (and other RF-edge) interactions on current drive. The effect of turbulence-induced refraction on HFS launch in DIII-D is quantified in this paper. Note that investigating RF-edge interactions for both HFS and LFS launch is prudent. The abundance of LFS launch data allows us to improve and validate our RF-edge models, which can then refine our predictions of HFS launch performance. In addition, understanding and mitigating RF-edge effects on LFS launch is in itself worth doing, since HFS launch is presently an unproven technology, and poses a greater engineering challenge.

In this paper, a model for synthetic SOL turbulence is developed in order to study turbulent scattering of LH waves in the plasma edge. The focus is on *edge* scattering for two reasons. First, edge turbulence ($\rho > 0.9$) comprises large density fluctuations: $\delta n/n \sim 10\%$ near the separatrix [20], approaching $\sim 100\%$ in the far-SOL [21]. Meanwhile, core turbulence ($\rho < 0.9$) typically consists of small ($\sim 1\%$) fluctuations [20]. Second, LH scattering is theorized to increase with the ratio $\zeta/k_\perp$ [8, 22], where ζ is the inverse characteristic scale-length of the turbulence, and $k_\perp$ is the LH wave-number component perpendicular to B. Given core turbulence is drift-wave-like, $\zeta\rho_s \sim 0.1$ [23], where ρ_s is the ion sound Larmor radius. In the electrostatic limit, $k_\perp \propto n_e^{1/2}$. This results in $\zeta/k_\perp \ll 1$ in the hot, dense core, and $\zeta/k_\perp$ approaching unity in the cooler, less dense edge. Thus, core scattering is negligible compared to edge scattering, even when accounting for the relatively large thickness of the core region.

The synthetic edge turbulence profile is coupled to the RTFP codes Genray/CQL3D [24,25] using the πScope scientific workbench [26]. Since this is a ray-tracing treatment, only the effects of turbulence-induced refraction are captured. Full-wave effects (ex. diffraction, partial-reflection,

and caustics) may also be important. Indeed, full-wave simulations of LH scattering with single blobs reveal significant back-scattering of the wave, even when the blob density is below the accessbility limit [27]. This partial-reflection, not accounted for in RTFP modelling, is shown to reflect $\sim 50\%$ of incident power back into the SOL for realistic blob parameters in C-Mod [28]. This should further increase RF-turbulence interactions (which further modify core damping profiles), and likely increase SOL collisional losses. Full-wave/Fokker-Planck treatment of LHCD is significantly more complex and expensive compared to RTFP models, and work in this field is ongoing [29–31]. State-of-the-art simulations only account for a single LH toroidal mode-number, when in reality, the launch spectrum is broad. This is especially problematic for modeling RF-turbulence interactions. The toroidal asymmetry of turbulence will further broaden the LH toroidal mode-number. For this paper, the ray-tracing treatment is employed for its relatively low computational cost, and the ease with which results can be interpreted.

1.2 Prior treatments of LH wave-scattering in SOL

Actually, there exist prior studies that employ modified ray-tracing treatments that include RF-turbulence interactions. So far, they have not been successful in explaining experimental current drive profiles. This would suggest that turbulence-induced refraction is *not* an important factor causing the spectral-gap. However, in light of improved measurements of SOL turbulence in recent years, the validity of these previous RF-turbulence models are brought into question.

Early ray-tracing work introduced a simple, analytic density fluctuation to the edge plasma, and demonstrated a significant modification to the LH resonance cone [7]. This treatment was improved upon by introducing a drift-wave-like turbulence profile to the edge, which resulted in significant angular diffusion of the LH wave-number during first-pass through the SOL [10]. This latter treatment failed to significantly modify the current profile in a weak-damping Tore Supra discharge.

The k-scattering model treats turbulence-induced refraction as a three-wave-interaction between (1) the incident LH wave, (2) the static turbulence, and (3) the scattered LH wave [8]. In assuming a particular spectral form for the turbulence (see Appendix B), a 90° scattering length for the incident LH wave, l_s, is derived. This scattering length is implemented as a Monte-Carlo ray scattering kernel in a ray-tracing scheme. While this treatment results in a significantly modified power deposition profile for C-Mod, the results were not able to reproduce experimental trends [9].

The models mentioned above assume spatially and temporally non-intermittent drift-wave-like turbulence. The previous ray-tracing study generated a turbulence profile by a superposition of sinusoidal waves with random phases. Similarly, the k-scattering model assumes the random-phase-approximation (RPA) in deriving the scattering kernel. This assumption may be adequate for core turbulence, but not for SOL turbulence. In reality, SOL turbulence is highly structured and intermittent, meaning the RPA is not valid. Probe measurements in the SOL reveal temporally intermittent spikes in ion-saturation current, signalling dense coherent structures. Statistical analysis of these probe measurements result in fluctuation probability distributions functions (PDFs) that fit a Gamma function [32]. Large positive skewness to the PDFs and large auto-correlation times in the far-SOL indicate highly dense, intermittent fluctuations. In contrast, Gaussian PDFs with shorter auto-correlation times inside the separatrix strongly indicate drift-wave-like turbulence. Optical and gas-puff imaging (GPI) confirm that SOL turbulence comprises of dense filamentary structures that extend along field lines and radially convect outwards

from inside the separatrix [33, 34]. GPI also confirms this turbulence is spatially intermittent; blobs are widely spaced out with low-density regions in between. Wave-scattering through this type of turbulence, as opposed to drive-wave-like turbulence, may be significantly different and could appreciably affect core ELD. In fact, slab model cases suggest that the angular diffusion of $\boldsymbol{k}_\perp$ is increased in the presence of blob-like turbulence compared to drift-wave-like turbulence. This is further discussed in Appendix C. Angular diffusion of $\boldsymbol{k}_\perp$ is even stronger as the blob-like turbulence becomes increasingly spatially intermittent. This finding has motivated the creation of synthetic density profiles that mimic real SOL turbulence. These profiles are coupled to the RTFP codes GENRAY/CQL3D in order to more accurately study the affect of turbulence-induced refraction of LH waves in the tokamak SOL, and its subsequent affect on current drive.

Care must be taken in applying the ray-tracing approximation in a turbulent (highly in-homogeneous) plasma. Heuristically, the ray-tracing approximation is adequate to model refraction given that $k_\perp \gg |(\boldsymbol{\nabla} n)/n| \approx (\delta n/n)\zeta$. Here, $\delta n/n$ is the relative blob density, and ζ is the inverse characteristic blob size. (Actually, this rough estimate for ray-tracing validity is not stringent enough, because we neglect strong coupling between the two perpendicular electric field components in a magnetized plasma [35]. This is discussed more in-depth in appendix A.) For example, consider the typical C-Mod outboard SOL, where $n \approx 10^{19} m^{-3}$ and $B = 4T$. A 4.6GHz LH ray with $N_{||} = 2$ will have $k_\perp \approx 700 m^{-1}$. One centimeter blobs (typical of C-Mod) result in $\zeta \approx 100 m^{-1}$. This limits the blob density fluctuation to $\delta n/n \ll 700\%$.

RF-turbulence interactions primarily lead to a broadening of the perpendicular wave-number ($N_\perp$) spectrum. Another RF-edge interaction only briefly mentioned so far is PDI. These interactions can lead to a parallel wave-number ($N_{||}$) up-shift. Previous studies have accounted for PDI effects by modifying the launched $N_{||}$ spectrum, and have had success matching experimental J_{tor} or HXR profiles [16,36,37]. The role of $N_{||}$ versus $N_\perp$-broadening in explaining the spectral-gap is an open question. In this paper, a modified $N_{||}$ launch spectrum is also modeled in GENRAY/CQL3D. In so doing, this question is investigated. Both SOL turbulence and this modified spectrum can be employed in GENRAY concurrently. In this way, the coupled effects that turbulence-induced refraction and PDI have on LHCD are modeled.

The remainder of this paper is split into six sections. Section 2 will describe the method for generating synthetic SOL turbulence, and how it is implemented in a C-Mod discharge modeled in GENRAY. Section 3 discusses the important differences in refraction through toroidally axisymmetric (2D) vs. field-following (3D) filaments. Section 4 briefly discusses the scheme for calculating steady-state current profiles in spite of rapid ray trajectory perturbations caused by the turbulent SOL. In section 5, the effect of blob turbulence parameters on current drive will be explored. In section 6, PDI effects will be included in the model via a tail in the $N_{||}$ launch spectrum. In this way, both PDI effects and turbulence-induced refraction are accounted for. In section 7, the blob model is applied to the planned DIII-D HFS LH launch [17] to predict the effect of SOL turbulence on current drive performance. Section 8 is reserved for discussion and summary. Lastly, the appendices discuss the validity of the blob-model, and its comparison to k-scattering treatment.

2 Methodology

The synthetic turbulence field is comprised of randomly-generated filaments that extend along field lines. Note that the word "blob" and "filament" are used interchangeably to refer to coherent structures in SOL turbulence, with "filament" usually used to emphasize the 3D, non-axisymmetric properties of these structures. The method to create this blob-field is a re-purposing and extension of previous work to generate 2D blobs in the poloidal plane for a synthetic GPI diagnostic [38]. Each realization of turbulence is a static (time-independent) field. This is a reasonable approximation given the turbulence frequency ($\sim$ 100 kHz) is much smaller than the LH wave frequency (4.6 GHz). The resulting frequency broadening of the LH wave is negligible ($\sim$ 1 MHz) and is not expected to significantly affect core ELD [39]. The following subsections discuss how the turbulence field is generated and implemented in GENRAY. Again, for a discussion on the validity of ray-tracing in blob-like density fluctuations refer to Appendix A.

2.1 Seed blob centers

A random point $\mathbf{X}_{i_0}(r_{i_0}, \phi_{i_0}, z_{i_0})$ in the SOL is chosen to seed the filament i, where $\mathbf{X}_{i_0}$ is the point from which the filament is extended radially and axially. r, ϕ, z are cylindrical coordinates. Next, the scalar values C_{i_0} and σ_{i_0} are generated. These are the blob intensity [in a dimensionless unit], and blob width [cm], respectively, in the poloidal plane $\phi = \phi_{i_0}$. Blobs are assumed to be circular in the poloidal plane.

σ_{i_0} is obtained from a PDF, the shape of which is a gamma function:

$$p(\sigma_{i_0}) = \frac{1}{\Gamma(\alpha)\beta^{\alpha}} \sigma_{i_0}^{\alpha-1} e^{-\frac{\sigma_{i_0}}{\beta}} \tag{1}$$

where α, β are the shape, scale of the gamma function, respectively. Increasing α will increase the spread in blob sizes. β is set to $\frac{\langle \sigma_b \rangle}{\alpha}$ to preserve the average blob size, $\langle \sigma_b \rangle$. The average blob-size is a free parameter. Experimentally, the average correlation length of blobs in the poloidal plane is found be 0.5-1.5 cm in C-Mod [34]. Following the Monte-Carlo method, a random uniform variable in the range $[0, 1]$ is generated for each filament, and a σ_{i_0} is assigned based on the cumulative distribution function (CDF) corresponding to eq. (1).
C_{i_0}, the so-called "intensity" of the blob, will dictate the density of the blob. It is dependent on blob-size, $C_{i_0}(\sigma_{i_0})$. It is dimensionless because it modifies the background density of the SOL. The absolute value of C_{i_0} is not important at the moment because it will be scaled, as will be seen shortly. Its relation to σ_{i_0}, however, is important, because this dictates how blob density scales with blob width. For this model, we assume $C_{i_0} \propto \sigma_{i_0}$, that is, blob density is proportional to blob size.

2.2 Generate each blob

The density of the filament is defined as:

$$\delta n_i(r, z, \phi - \phi_{i_0}) = C_i(C_{i_0}, l_{||}) e^{-\frac{(r - r_i(\mathbf{X}_{i_0}, \phi - \phi_{i_0}))^2 + (z - z_i(\mathbf{X}_{i_0}, \phi - \phi_{i_0}))^2}{\sigma_i(\sigma_{i_0}, l_{||})^2}} \tag{2}$$

where coordinates $(r_i(\mathbf{X}_{i_0}, \phi - \phi_{i_0}), z_i(\mathbf{X}_{i_0}, \phi - \phi_{i_0}))$ prescribes the axis of the filament, and are determined by following the field-line that passes through point $\mathbf{X}_{i_0}$. In this sense, the filament is "field-line following". The effect of filament shear due to the shearing of neighboring field-lines is

neglected. $l_{||}$ is the distance along the field-line from point $\mathbf{X}_{i_0}$ to point $(r_i, z_i, \phi - \phi_{i_0})$. In making C_i and σ_i dependent on $l_{||}$, the filament can be tapered along the parallel direction. In this model:

$$C_i, \sigma_i \propto \begin{cases} cos(\pi \frac{l_{||}}{L_{max}}) & l_{||} \leq L_{max}/2 \\ 0 & l_{||} > L_{max}/2 \end{cases} \tag{3}$$

where L_{max} is some finite length so that filaments do not extend infinitely in the parallel direction. SOL measurements show that $L_{||,fil.} \gg L_{\perp,fil.}$ [40]. Correspondingly, we choose $L_{max} = 4$m, while $\sigma_i \sim 1$cm. Each filament is extended along the field line in the parallel (+) and counter-parallel (−) direction until a) $l_{||}^{\pm} = L_{max}/2$ or b) the filament impinges on the vessel wall.

The unscaled blob field is:

$$\Delta n(r, z, \phi) = \Sigma_i \delta n_i(r, z, \phi - \phi_{i_0}) \tag{4}$$

The number of blobs in the field depends on the prescribed packing fraction, f_p, of the turbulence. It is an inverse measure of the blob-field spatial intermittency. This packing fraction is defined as the volumetric fraction of the SOL inhabited by blobs, $f_p = \frac{1}{V_{SOL}} \Sigma_i V_{fil.,i}$. Where, V_{SOL} is the volume in which filaments may exist.

$$V_{fil.,i} = \pi \int_0^{l_{||}^+} + \int_0^{l_{||}^-} [(2ln(2)^{1/2} \sigma_i(l_{||}))^2 dl_{||}] \tag{5}$$

where $2ln(2)^{1/2}\sigma_i$ is the full-width half-max of the filament's density profile in the poloidal plane (FWHM$_i$). After each filament is generated, f_p is recalculated. Filaments continue to be generated until the prescribed f_p is reached. GPI measurements in NSTX and Langmuir probe measurements in ASDEX Upgrade indicate $f_p \approx 0.1 - 0.2$ in L-mode plasmas [41, 42], at least in the far-SOL. GPI measurements in C-Mod indicate $f_p \sim 0.05$ [43], though it is unclear at what radial location this is calculated.

Note that, if we were to model toroidally axisymmetric (2D) turbulence, then $(r_i(\mathbf{X}_{i_0}, \phi), z_i(\mathbf{X}_{i_0}, \phi)) \rightarrow (r_{i_0}, z_{i_0})$, $C_i(l_{||}) \rightarrow C_{i_0}$, and $\sigma_i(l_{||}) \rightarrow \sigma_{i_0}$. The filaments would be annular. The definition of packing fraction would reduce to $f_p = \frac{\pi}{A_{SOL}} \Sigma_i \text{FWHM}_i^2$, where A_{SOL} is the cross-sectional area of the SOL in the poloidal plane. Figure 1 shows two example fields of randomly generated blobs in a 2D rectilinear grid. The average blob size and the number of blobs in the field is dependent on the specified $\langle \text{FWHM} \rangle$ and f_p.

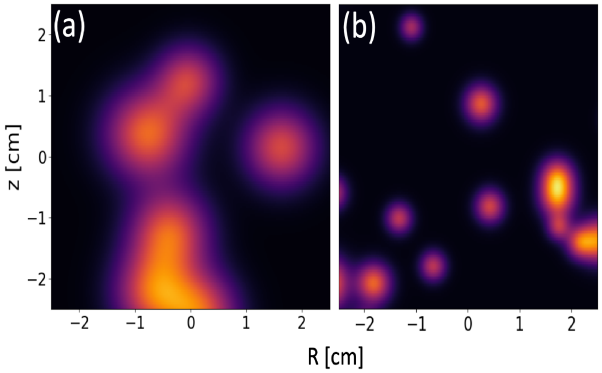

Figure 1: Blob field in a poloidal plane with (a) $\langle FWHM \rangle = 1$ cm, $f_p = 0.6$, and (b) $\langle FWHM \rangle = 0.5$ cm, $f_p = 0.25$. Blobs are in orange, while black indicates the absence of blobs.

2.3 Normalizing the blob field

The SOL density is:

$$n(r,z,\phi) = n_0(r,z)\Sigma_i \delta n_i(r,z,\phi-\phi_{i_0}) = n_0(r,z)\Delta n(r,z,\phi) \tag{6}$$

where Δn, a positive scalar field, is the blob-field modification to the background density.

A constant offset is subtracted from the blob field ($\Delta n(r,z,\phi) \rightarrow \Delta n(r,z,\phi) - a$) so that its spatial average, $\langle \Delta n \rangle$, is zero. Next, the blob field is scaled by a constant ($\Delta n(r,z,\phi) \rightarrow b\Delta n(r,z,\phi)$) so that $\langle |\Delta n| \rangle = 1$. The blob field is scaled in this specific way so that each filament is denser than the local background density, while the absence of a filament results in a local density slightly lower than the background ($0 < \Delta n < 1$). In imposing this method of normalization, filaments that are density *holes* do not exist in this model. This is generally true for the far-SOL, since measured fluctuation distributions in this region have large positive skewness [32].

2.4 Spatial dependencies of the SOL profile

Lastly, the filament profile is modified to approximate the spatial variation in turbulence intensity measured in experiment. The time averaged turbulence intensity is defined as $\langle |\Delta n| \rangle_t = f(\rho)g(\theta)$, where f and g are arbitrary functions of normalized radius $\rho \sim \psi_{tor}^{1/2}$ and poloidal angle θ, respectively. ψ_{tor} is the toroidal flux. $\langle ... \rangle_t$ indicates a time-averaged quantity, and is equivalent to averaging over infinite realizations of the blob-field. As previously discussed, the Δn field was scaled such that $\langle |\Delta n| \rangle = 1$. $f(\rho)g(\theta)$ introduces a local deviation of turbulence intensity from unity: $\Delta n \rightarrow 1 + \frac{\Delta n - 1}{|\Delta n - 1|} f(\rho)g(\theta)$.

For our purposes, f is chosen to be of an exponential form

$$f(\rho) = \begin{cases} 0 & \bar{\rho} < 0 \\ (\delta n_g/n) \times \frac{e^{\bar{\rho}}-1}{e-1} & 0 < \bar{\rho} < 1 \\ \delta n_g/n & \bar{\rho} > 1 \end{cases} \tag{7}$$

where $\bar{\rho} = (\rho - \rho_{min})/(\rho_{grill} - \rho_{min})$. ρ_{min} sets the minimum radial location for the presence of blobs, and in this study is set at 0.95. ρ_{grill} is defined as the radial location of the grill, and $\delta n_g/n$ as the user-input for turbulence intensity at the grill. This mimics the tendency for the normalized intensity of SOL turbulence to monotonically increase with radius [18, 34]. Large poloidal variations also exist in SOL turbulence. The LFS is rather turbulent due to bad curvature, and the HFS SOL is relatively quiescent [18, 19]. Correspondingly, we define $g(\theta) = cos^2(\theta/2)$ so that $\langle |\Delta n| \rangle_t$ is maximum at the LFS mid-plane, and zero at the HFS mid-plane.

2.5 Implementing SOL turbulence into Alcator C-Mod discharge modelled in GENRAY

An Alcator C-Mod discharge (overview in Fig. 2) is modeled in GENRAY/CQL3D to study the effect of turbulence on LH wave propagation and current drive (CD) in a multi-pass scenario. This upper single-null L-Mode discharge, with $\overline{n_e} = 0.52 \times 10^{20}$ m^{-3}, $I_p = 530$ kA, and B=5.4 T, achieves non-inductive current drive with $P_{LH} = 850$ kW launched at $N_{||} = -1.6$ and 4.6 GHz [44]. At t=1.1 sec, the loop voltage is zero. Closer inspection of the Motional Stark Effect (MSE) constrained current profile [30], over the period t=1.0-1.4 sec, confirm that the current

profile is close to steady-state. Therefore, the DC electric field and Ohmic current is small and has been neglected. Doing so avoids the potential problem of "slide-away" fast electron tails in CQL3D caused by the synergy of ELD and DC electric field [14].

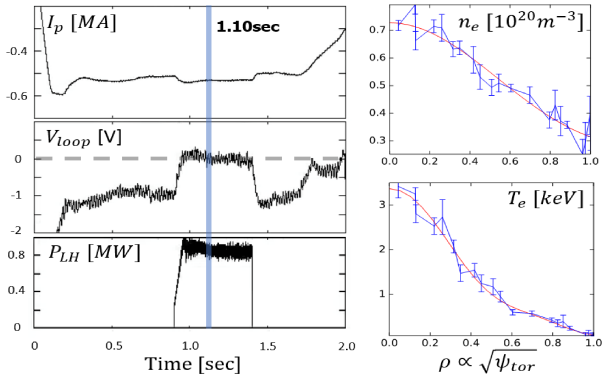

Figure 2: Summary of Alcator C-Mod upper single-null L-Mode discharge #1101104011. $\overline{n_e} = 0.52 \times 10^{20}\ m^{-3}$, $I_p = 530$ *kA, and B=5.4 T. At t=1.10 sec, current is fully driven by 850 kW LH power launched at* $N_{||} = -1.6$. *Electron density* (n_e) *and temperature* (T_e) *profiles show experimental data from Thomson scattering (blue), and the fit profile (red) used in GENRAY/CQL3D runs.*

The background SOL is modeled as an exponentially decaying density (n) and temperature (T) field with e-folding lengths $\lambda_{SOL_n} = \lambda_{SOL_T} = 7$ mm at the outer mid-plane. While λ_{SOL_T} is kept constant, λ_{SOL_n} varies poloidally, and increases to 15 mm at $\theta = \pi/2$. This is done to approximately model the widened SOL at the upper single-null. At the vessel wall, the background density rapidly falls below the cutoff to force ray reflection.

A 32 channel HXR diagnostic [45] in C-Mod provides HXR count-rate profiles that can be compared with the synthetic HXR diagnostic in CQL3D. As mentioned previously, an MSE diagnostic also provides MSE-constrained equilibrium and current profiles in the core. The latter enables direct comparison to the current profile calculated in CQL3D.

The 3D blob-field is superimposed with the background density as described in Eq. (7). Figure 3a shows the final n_e profile for a specific toroidal angle. Figure 3b and 3c are enlarged to show the LFS and HFS SOL for the same slice. Note that the blob field is more quiescent in the HFS. Figure 3d and 3e show a LFS and HFS slice toroidally displaced by $\pi/3$ rad. Compared to Fig. 3b and 3c, these blob fields differ because each filament is field-line following.

In GENRAY, the blob-field is input as a $M_r \times M_z \times M_\phi$ array, where M_i indicates the number of grid points in the i-direction. $M_r = M_z = 1000$ and $M_\phi = 150$. A lower resolution is used in the toroidal direction since density gradients along ϕ are smaller than in the r, z directions. As per the ray-tracing treatment, the evolution of a ray trajectory depends on the local density and density gradient. These values are calculated using a 3D spline interpolation scheme.

3 Ray propagation through 2D vs 3D turbulence

The task of creating field-following filaments, as opposed to simply axisymmetric blobs, has been undertaken because the latter field does not conserve the correct wave-vector components of the LH ray during refraction. Toroidally axisymmetric turbulence introduces a finite parallel density

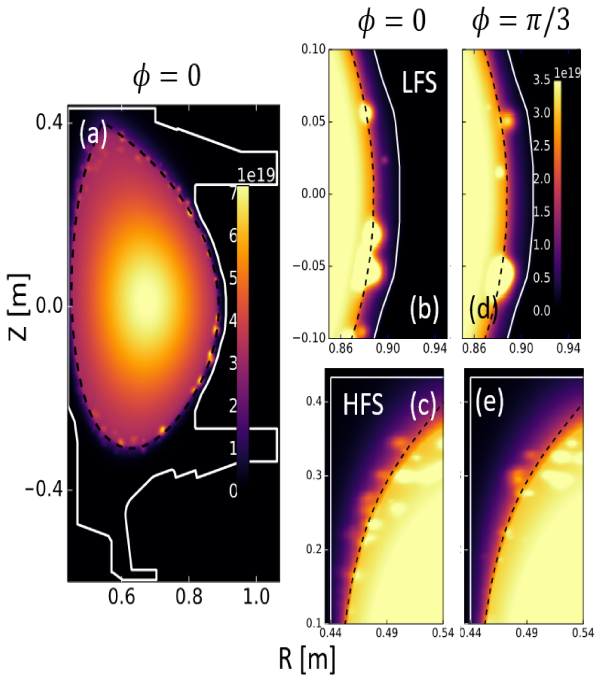

Figure 3: One realization of SOL turbulence in C-Mod discharge. n_e poloidal slice at $\phi = 0$ for (a) whole plasma, (b) low-field side, and (c) high-field side. Poloidal slice at $\phi = \pi/3$ for (d) low-field side, and (e) high-field side. Blob parameters: $\delta n/n_g = 0.5, \langle FWHM \rangle = 1.0$ cm, $f_p = 0.6$

gradient, $\partial_{||} n$, in the presence of a non-zero B_θ, while keeping toroidal density gradient $\partial_\phi n = 0$. Figures 4b and 4c show $N_{||}$ and toroidal mode-number, m, evolution during the first-pass through the SOL. In the presence of axisymmetric filaments, it is evident that $N_{||}$ changes, and m is conserved. Conversely, field-following filaments minimizes $\partial_{||} n$ (in the limit $L_{max} \to \infty$), while introducing a non-zero $\partial_\phi n$. As shown in Fig. 4b and 4c, this conserves $N_{||}$ and changes m of a ray refracting from a filament. In the multi-pass regime in a high inverse aspect-ratio ($\epsilon \equiv a/R$) device, rays are highly stochastic. Small changes in wave-vector during the first-pass through the SOL can significantly affect where a ray damps (see Fig. 4a). Simulating LH launch through 2D vs. 3D turbulence therefore also leads to quantitatively different core power deposition, current, and HXR profiles. This is seen in Figure 5 where 2D (dashed blue line) turbulence results in larger on-axis peaking than a similar case with 3D turbulence (solid blue line). (How these profiles are calculated is explained in Section 4.) This is attributed to a significant $N_{||}$ up-shift for rays interacting with axisymmetric blobs in the 2D case, leading to strong on-axis damping once these rays reach the core. This strong $N_{||}$ up-shift (caused by large $\partial_{||} n$) is not expected to occur in experiment, where blobs are field-following. This motivates the modeling of field-following turbulence, rather than axisymmetric turbulence, for RTFP studies.

Recent full-wave simulations of LH propagation in the edge have employed axisymmetric SOL filaments. Strong diffraction effects are expected to significantly modify the resonance cone [28]. In full-wave studies, the argument against using axisymmteric turbulence is similar. In an axisymmteric case, diffraction will broaden the $N_{||}$ spectrum. In a field-following case, only the $N_\perp$ spectrum is broadened.

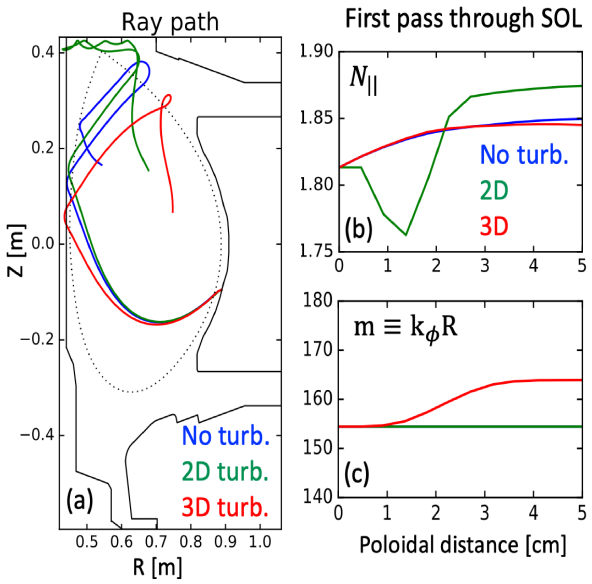

Figure 4: (a) Ray trajectories in C-Mod for different SOL turbulence models. $N_{||_0} = -1.81$. (b) $N_{||}$ and (c) m (toroidal mode number) evolution of rays during first-pass through SOL. I_p and B_{tor} run clockwise when tokamak viewed from top. Therefore, the forward lobe travels clockwise in poloidal projection.

4 Calculating steady-state current drive in the presence of a turbulent SOL

The Fokker-Planck solver CQL3D is used to evolve the electron distribution function in the presence of ELD. Particular care must be taken in evolving the electron distribution when ray-trajectories are perturbed by a turbulent SOL. As described in the 2011 RTFP study by Peysson et al. [10], when the turbulence turnover time $\tau_{turb} \sim 10^{-5}$s is much smaller than the fast electron slowing-down time $\tau_{fe} \sim 10^{-3}$s, the ray trajectories will be significantly perturbed before the current profile has appreciably evolved. In effect, the quasi-linear diffusion coefficient, D_{ql}, will rapidly fluctuate in phase-space relative to the current evolution time. Proper evolution of the electron distribution likely requires taking small time steps, Δt, in CQL3D such that $\tau_{turb} < \Delta t < \tau_{fe}$. At each new time step, the SOL density is updated with a new realization of filaments, and the ray-trajectories are correspondingly updated in GENRAY. For time step $t = p\Delta t$, where p is an integer, rays will Landau damp on (and consequently evolve) the electron distribution calculated at $t = (p-1)\Delta t$, which resulted from the previous set of damped rays. Therefore, ELD along the ray-trajectories for the present turbulence realization will be affected by ELD along the ray-trajectories for the *previous* turbulence realizations. The effect of this hysteresis is captured with increasing accuracy as $\Delta t \to \tau_{turb}$. For the remainder of this paper, this workflow of updating the ray-trajectories at Δt increments while evolving the Fokker-Planck calculation of the electron distribution function is called the "hysterisis model".

It is not clear, *a priori*, what Δt should be for sufficiently converged current profiles. This was studied numerically in GENRAY/CQL3D by scanning $\Delta t = [0.1\tau_{fe}, 10\tau_{fe}]$ for the above discharge and fixed turbulence parameters ($\langle \text{FWHM} \rangle = 1$cm, $\delta n_g/n = 0.25$, $f_p = 0.25$). The final current profiles were taken as a rolling average once a) I_{LH} saturated and b) more than 50 time steps were taken. Note than in the case of large time steps, ex. $\Delta t = 10\tau_{fe}$, the current profile fully reaches steady-state at each time step. Information about the previous steady-state electron distribution

function is lost and, in averaging these current profiles, the ergodic hypothesis is assumed. Here, the term "ergodic hypothesis" is used in the context of computational physics, where it denotes the assumption that the time-averaged behavior of a system is equivalent to the average of a statistical ensemble. Remarkably, the power deposition and HXR profiles did not differ significantly as Δt was scanned. Another method to calculate steady-state current drive is to simply average the D_{ql} resulting from several realizations of ray-trajectories. This method is another interpretation of the ergodic hypothesis, and again matched results from the hysteresis model. A similar result was found in a RTFP study for Tore Supra [16]. In summary, while there is no strong defense for the validity of the ergodic hypothesis *a priori*, in practice it provides similar results to the hysteresis model, at least for the specific background, turbulence, and launch parameters tested. This may not hold true for other plasma and RF parameters, so further investigation is required. For the remainder of the paper, the hysteresis model is used, with $\Delta t \approx \tau_{fe}$.

5 Effect of turbulence parameters on current drive

In GENRAY, 1MW of LH power is launched in the low-n_e non-inductive C-Mod plasma at $N_{||} = -1.6$ (the same peak $N_{||}$ launched in experiment). The LH grill is modelled as 4 poloidally spaced launch points, which approximates its 4-way splitter design. Rays in the forward lobe are launched at sufficiently low $N_{||}$ that multiple passes are needed to fully damp. The effect of ray stochasticity on long ray-paths require a large ray density for a well converged quasi-linear calculation of J_{tor} [46]. Correspondingly, 340 rays are launched in the forward lobe centered at $N_{||} = -1.6$, with 15% of launched power directed in the backward lobe centered at $N_{||} = 6$. This high-$N_{||}$ back lobe damps strongly on first-pass near, so relatively few rays are modeled (60 are used).

The steady-state current profile is calculated in CQL3D using the method described in section 4. A scan of f_p is conducted, keeping $\delta n_g/n$ and $\langle \mathrm{FWHM} \rangle$ fixed (Fig. 5). The presence of turbulence in the SOL greatly smooths the off-axis power and current deposition profiles. On-axis current also increases. The HXR profile "shoulder" is significantly mitigated.

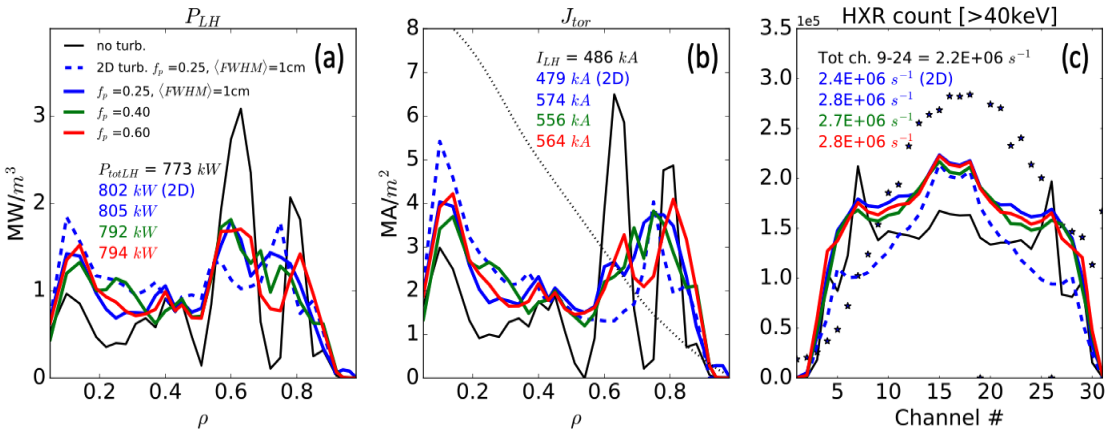

Figure 5: Scan of f_p. CQL3D calculated (a) power density, (b) current density, and (c) HXR profiles for 850 kW LH power launched at $N_{||} = -1.6$. Dashed black line is experimental J_{tor}. Black stars are experimental HXR count. $\delta n_g/n = 0.25$, $\langle FWHM \rangle = 1$ cm.

Remarkably, the packing fraction has little effect on the steady-state profiles. This is in contradiction to slab model results, where decreasing f_p resulted in increased wave scattering (see Appendix

B). This is possibly due to the difference in turbulent layer widths in the slab model ($\approx$ 15cm) versus the tokamak SOL ($\approx$ 1cm). In the slab model, each ray could interact with multiple blobs during its pass through the turbulent layer. In this case, the rotation of $k_\perp$ is akin to a random walk. In C-Mod, the SOL width is comparable to the filament width ($\lambda_{SOL_n} \sim \langle FWHM \rangle$). At first-pass through the SOL, turbulence-induced refraction of a ray is approximately a binary process, and therefore quite different from the slab case. The fact that f_p has little effect on steady-state profiles is good news for modeling ray trajectories through turbulent plasmas. The WKB approximation sets a maximum limit on density in-homogeneity, where

$$\boldsymbol{\nabla}_\perp n \propto (\delta n_g/n)\langle \mathrm{FWHM} \rangle^{-1} f_p^{-1} \tag{8}$$

if only the blobs are considered. Given that $\boldsymbol{\nabla}_\perp n$ must stay below some maximum value (see Appendix A), f_p can be artificially increased, allowing the study of ray refraction at higher $\delta n_g/n$ and smaller $\langle$FWHM$\rangle$.

Increasing $\delta n_g/n$ significantly affects steady-state profiles relative to the case with no turbulence (Fig. 6). This is consistent with the k-scattering model, where the angular diffusion coefficient $D_{\theta\theta} \propto \langle |\Delta n| \rangle^2$ [35] (see Appendix C). Near-axis ($\rho < 0.5$) current increases with $\delta n_g/n$. At $\delta n_g/n = 0.4$, the current profile in nearly flat for $\rho < 0.9$. Correspondingly, the HXR profile shoulders are completely mitigated.

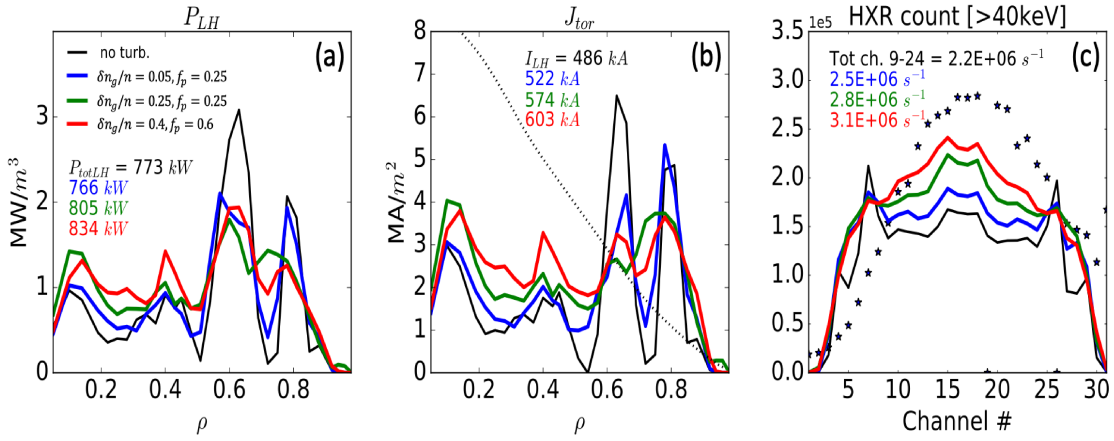

Figure 6: Scan of $\delta n_g/n$. CQL3D calculated (a) Power density, (b) current density, and (c) HXR profiles for 850 kW LH power launched at $N_{||} = -1.6$. Dashed black line is experimental J_{tor}. Black stars is experimental HXR count. $\langle FWHM \rangle = 1$ cm.

Decreasing $\langle$FWHM$\rangle$ further smoothes steady-state profiles (Fig. 7). Again, this is consistent with the k-scattering model, where $D_{\theta\theta} \propto \langle \mathrm{FWHM} \rangle^{-1}$ [35]. The J_{tor} profile shape is still significantly different from the experimental profile.

5.1 Robustness of calculated steady-state profiles

Recall that another major issue with RTFP modeling is the sensitivity of results to small changes in core profiles [14, 16]. Steady-state profiles, with and without SOL turbulence, are calculated with the background core density profile scaled $\pm$10% (Fig. 8). Without SOL turbulence, the resulting current profile is highly sensitive to changes in core density. This is due to the stochastic nature of ray trajectories in a multi-pass regime. Furthermore, driven current should inversely

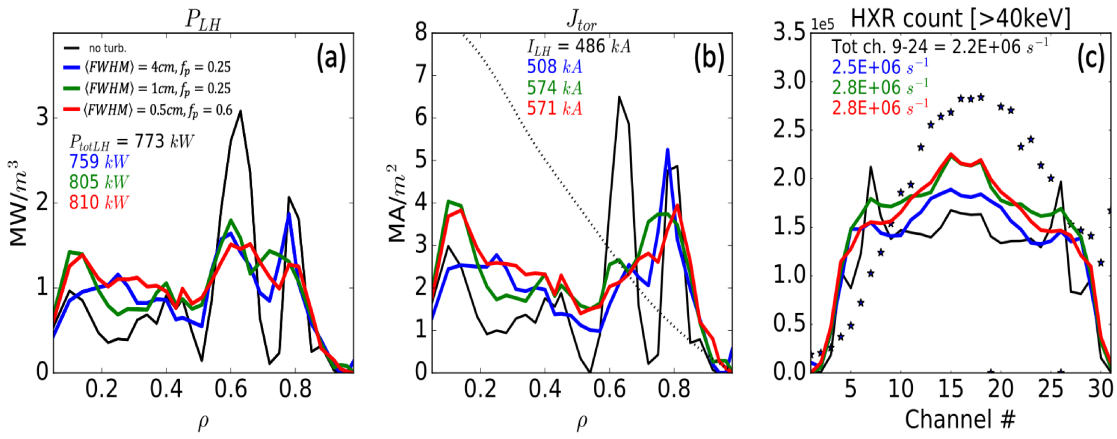

Figure 7: Scan of ⟨FWHM⟩. CQL3D calculated (a) Power density, (b) current density, and (c) HXR profiles for 850 kW LH power launched at $N_{||} = -1.6$. Dashed black line is experimental J_{tor}. Black stars is experimental HXR count. $\delta n_g/g = 0.25$.

scale with collisionality, so that, roughly, $I_{LH} \propto \overline{n_e}^{-1}$. With no SOL turbulence, this trend is not recovered. In contrast, cases with SOL turbulence are much more robust to changes in core density, and I_{LH} roughly scales with inverse $\overline{n_e}$. This suggests that turbulence induced refraction broadens the $\boldsymbol{k}_\perp$ spectrum of the rays in each pass through the SOL, making their averaged trajectories less sensitive to the background density profile.

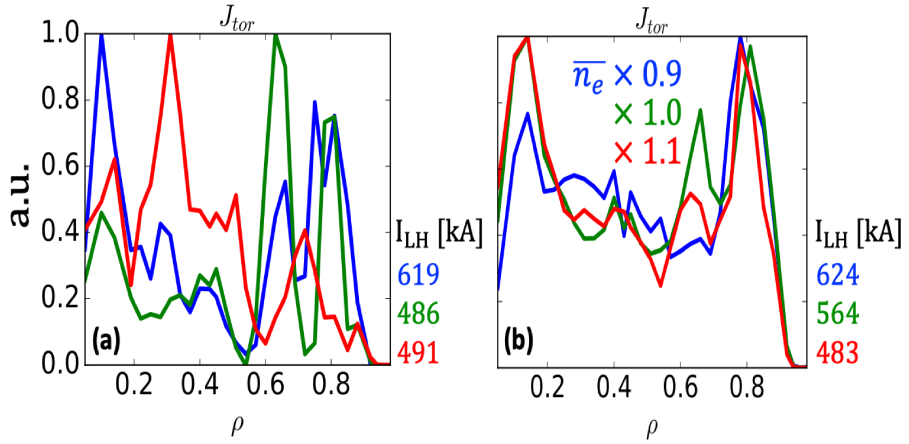

Figure 8: n_e scan to test robustness of GENRAY/CQL3D results. Normalized J_{tor} profiles (a) without turbulence, and (b) with $\delta n_g/n = 0.25, \langle FWHM \rangle = 1$ cm, $f_p = 0.6$.

The increased diffusion of ray-trajectories in phase-space due to turbulence is more clearly shown by plotting these trajectories in ρ - $N_{||}^{-1}$ space (Fig. 9). The density of rays in phase-space is an approximate proxy for D_{ql}. Therefore, turbulence acts to diffuse D_{ql} in phase-space, resulting in smoother, more robust current-drive profiles. This is most evident near-axis (refer to yellow box in Figure 9).

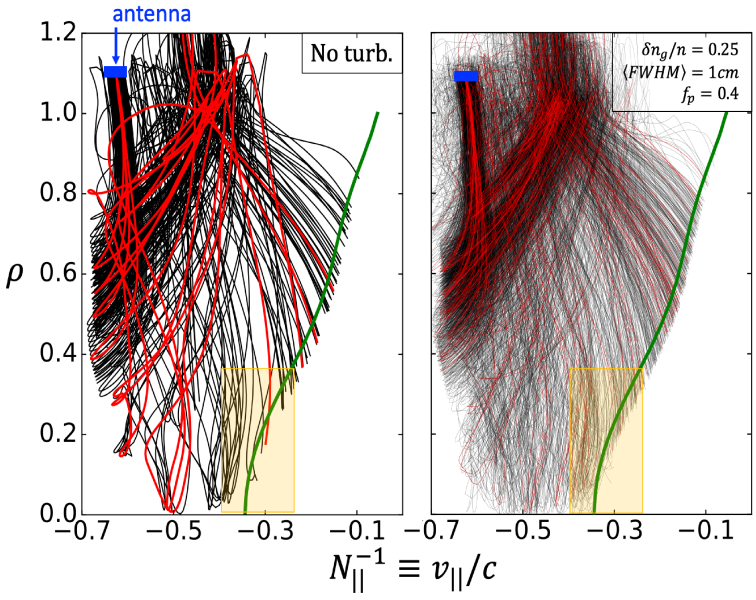

Figure 9: Ray trajectories in phase-space for (left) no turbulence case and (right) with turbulence case. In turbulence case, ray-trajectories due to 10 different realizations of turbulence are plotted. Red lines are rays with maximum initial power. Black lines are top 10% of rays with highest initial power. Green line is ELD resonance condition: $\left|N_{||}^{-1}\right| \equiv \left|v_{||}\right|/c \approx 3v_{th_e}/c$*, where* v_{th_e} *is the electron thermal velocity.*

6 Turbulence-induced refractive effects combined with modified waveguide spectra

Following the work of Cesario et al. [36] and Decker and Peysson [16], a tail is added to the $N_{||}$ launch spectrum of the forward lobe in an attempt to include the effects of PDI, and to recover current profiles that match experiment (Fig. 10). Note that since blob-like turbulence is field-following, RF-turbulence interactions conserve $N_{||}$. Therefore, the $N_{||}$ tail is not caused by turbulent scattering, and is due to a separate physical mechanism, in this case PDI.
It is hypothesized that the coupling of the high $N_{||}$ tail and the SOL blob model may help to further drive on-axis current and create a smooth, monotonic J_{tor} profile. As shown in Fig. 10, this tail spectrum is modeled as a superposition of three additional lobes centered at $N_{||}$ = -2, -2.5, and -3. Two hundred rays model the main lobe, while 340 rays model the sub-lobes. The fraction of launched power in the tail, P_{tail}/P_{tot}, is scanned to determine the extent of pump depletion required to recover the experimental J_{tor} profile.

6.1 P_{tail} scan

The scan of P_{tail}/P_{tot} was modeled in GENRAY/CQL3D, with and without SOL turbulence. For the no-turbulence cases (Fig. 11a and 11b), increasing fractional power to the tail results in a higher total LHCD. This trend saturates near $P_{tail}/P_{tot} = 0.5$, consistent with previous results [37]. The current profile shape also increasingly matches experiment as P_{tail}/P_{tot} increases, due to high $N_{||}$ rays in the tail preferentially damping near-axis and during the first-pass. An on-axis current peak is recovered at $P_{tail}/P_{tot} = 0.5$, and is also consistent with previous $N_{||}$-tail RTFP modeling [37]. However, doubts remain over whether a 50% pump depletion is really present in a low density C-Mod discharge [47].

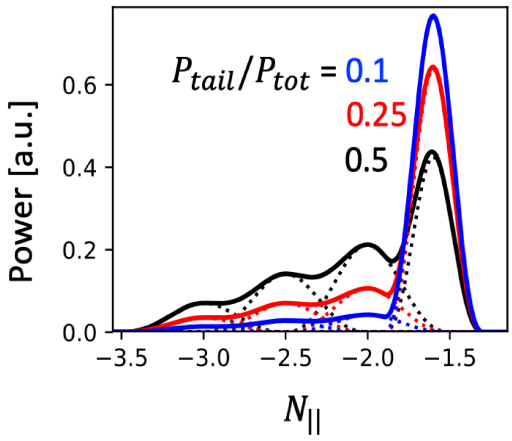

Figure 10: Modified $N_{||}$ launch spectrum of the forward lobe ($N_{||_{peak}} = -1.6$.) with up-shifted $|N_{||}|$ tail. Total forward launch spectrum (solid lines) is modeled with 4 sub-lobes (dashed lines) in GENRAY.

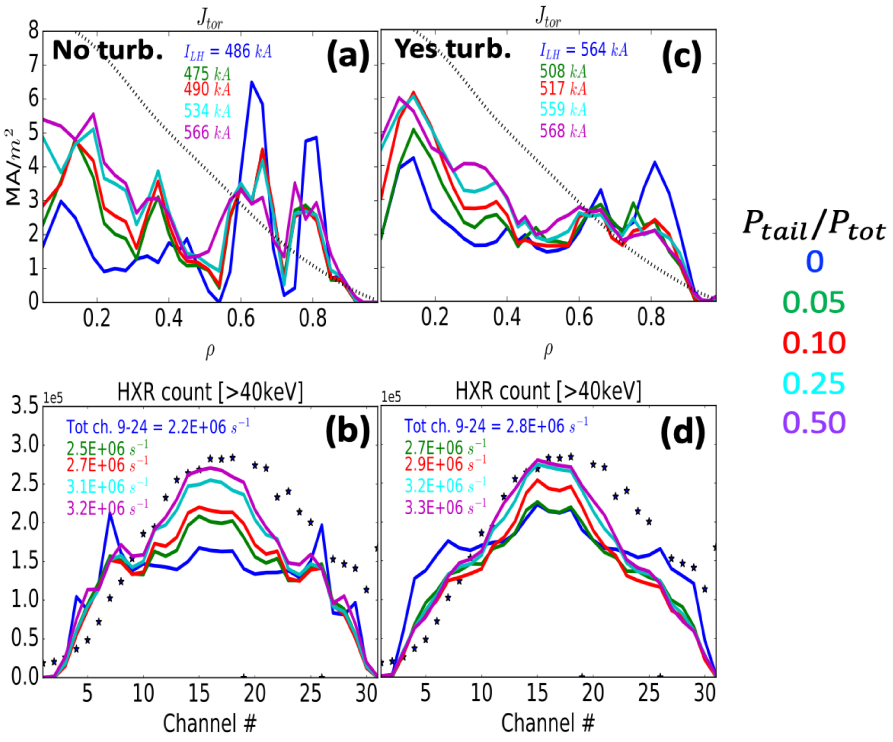

Figure 11: Scan of P_{tail}/P_{tot}. a) J_{tor} and b) HXR profiles without turbulence. c) J_{tor} and d) HXR profiles with turbulence parameters: $\delta n_g/n = 0.25$, $\langle FWHM \rangle = 1$ cm, $f_p = 0.6$. Experimental J_{tor} in dashed line. Experimental HXR profile in black stars.

The cases with an $N_{||}$-tail *and* SOL turbulence are able to match the experimental HXR profile shape with $P_{tail}/P_{tot} \sim 0.1 - 0.25$ (Fig. 11c and 11d). The J_{tor} profile shape is also matched to a lesser extent. This better match to experiment is largely due to refraction from SOL turbulence resulting in more of the rays in the tail spectra accessing the core during first-pass. This leads to greater first-pass damping near-axis. The current "valley" seen at $\rho = 0.5$ is also mitigated due to this effect. The calculated I_{LH} and total HXR count are still under-predicted for $P_{tail}/P_{tot} \sim 0.1, 0.25$. Overall, the $N_{||}$-tail and SOL turbulence model still result in significantly under-predicted on-axis current and a J_{tor} profile that is too broad (over-predicted for $\rho > 0.6$).

On possible cause of this remaining discrepancy is full-wave effects. Significant back-scatter of LH power from blobs [28] will further modify the current profiles shown in Fig. 11. However, these profiles now are monotonically decreasing and smooth, as seen in experiment. Predicted HXR profile shape is in excellent agreement with measurements. This discrepancy in agreement between HXR and current profile is due to the former being a chordal measurement.

The robustness of results with $P_{tail}/P_{tot} = 0.1$ is tested by scanning the background density $\pm 10\%$ (Fig. 12). Again, the presence of SOL turbulence greatly increases the robustness of J_{tor} profiles.

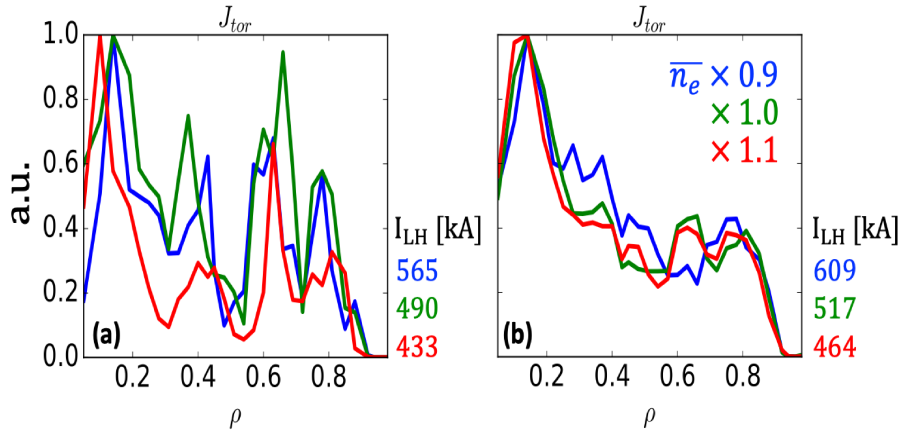

Figure 12: n_e scan to test robustness of GENRAY/CQL3D results with $P_{tail}/P_{tot} = 0.1$. Normalized J_{tor} profiles (a) without turbulence, and (b) with $\delta n_g/n = 0.25$, $\langle FWHM \rangle = 1$ cm, $f_p = 0.6$.

7 Impact of SOL turbulence on DIII-D HFS LH launch

The preceding sections focused on RF-scattering in the multi-pass regime in C-Mod. Now, attention is given to the HFS launch-scenario in DIII-D, which is predicted to result in single-pass damping for two reasons. First, LH waves have improved accessibility due to higher B [48]. Second, these ways strongly damp off-axis due to high T_e (made possible by neutral-beam heating). The HFS SOL is relatively quiescent, which should result in less LH wave scattering. However, even with artificially high HFS turbulence, the effect of wave-scattering on core-damping may be small. This is because ray-trajectories are shorter in the single-pass regime, and therefore less sensitive to perturbations caused by turbulence. This hypothesis is tested by modelling a DIII-D HFS LH launch scenario over a wide range of HFS SOL turbulence intensities. The modeled plasma is a high q_{min} discharge with $B_0 = 1.6$ T, $n_{e_0} = 6 \times 10^{19}$ m^{-3}, and $T_{e_0} = 4.4$ keV (see [17] for core profiles). In GENRAY, 1.6 MW of LH power at 4.6 GHz is launched from four poloidal points centered slightly under the mid-plane [49]. A schematic of the launcher location in DIII-D is shown in [17]. Fifty rays are launched in the forward lobe at $N_{||} = -2.7$, with 30% of power launched in 16 rays in the backward lobe at $N_{||} = 8$. The launcher is positioned 3 cm from the separatrix.

As expected, with a quiescent SOL, HFS launch results in strong single-pass damping (see Fig. 13a). For the turbulence cases, the blob-field fluctuation intensity is modeled with no poloidal variation: $g(\theta) = 1$. (Note that the previous form, $g(\theta) = cos^2(\theta/2)$, forced a quiescent SOL near the HFS mid-plane no matter the radial variation $f(\rho)$.) The form for $f(\rho)$ is kept unchanged

and turbulence intensity is scanned: $\delta n_g/n = [0.05, 0.75]$ while other turbulence parameters are kept constant ($\langle \text{FWHM} \rangle = 1.5$ cm and $f_p = 0.25$). Figure 13b-e show LH ray trajectories through SOL turbulence at various $\delta n_g/n$. Note that, in each figure, trajectories for only one realization of turbulence are shown. Nevertheless, they are typical trajectories at the given $\delta n_g/n$. For $\delta n_g/n \geq 0.4$, some rays, on refraction from a blob, are rotated away from the core such that they damp collisionally near the lower-null. In all cases, the majority of rays Landau damp strongly on first-pass.

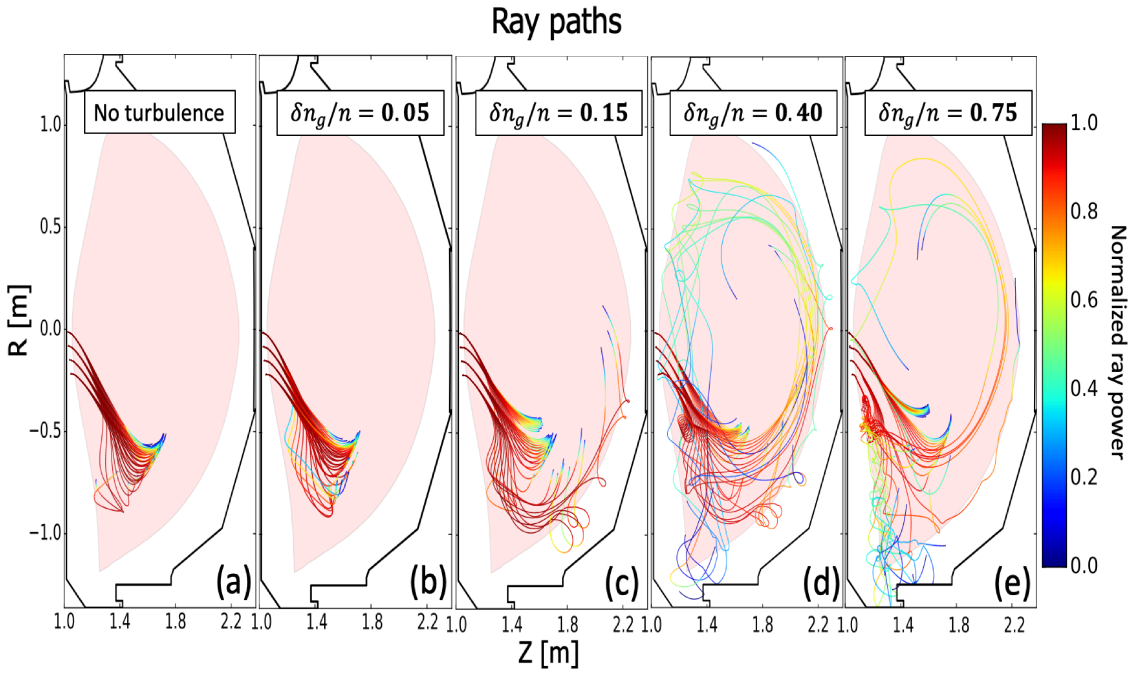

Figure 13: Rays paths in DIII-D for quiescent SOL (a) and turbulent SOL with $\delta n_g/n$ =0.05, 0.15, 0.4, and 0.75 (b-e). In figures b-e, ray paths result from a single turbulence realization. Ray color denotes power in ray normalized to initial power. Forward lobe launched at $N_{||} = -2.7$. B_{tor} and I_p run counter-clockwise when tokamak viewed from top. Therefore, forward lobe travels counter-clockwise in poloidal projection. Backward lobe at $N_{||} = 8$ Landau damps immediately near separatrix.

The $\delta n_g/n$ scan reveals that "high" turbulence intensity ($\delta n_g/n \gtrsim 0.15$) in the HFS can significantly affect the current profile (Fig. 14). With no turbulence, LH waves are expected to drive off-axis current peaked at $0.6 < \rho < 0.8$, and should achieve $J_{tor} > 0.3\text{MA}/m^2$ at $\rho \approx 0.7$. With increasing $\delta n_g/n$, this peak is broadened and shifted inward to $\rho \approx 0.55$. Notably, even at a large $\delta n_g/n = 0.40$, total off-axis current drive (where "off-axis" denotes the region $0.5 < \rho < 0.9$) only drops $< 10\%$ compared to the no turbulence case.

Fortunately, due to the ballooning nature of SOL turbulence, HFS turbulence intensity is measured to be $\sim 10\times$ lower than on the LFS. GPI measurements in C-Mod reveal that $\langle \Delta n \rangle \approx 0.05$ in the HFS SOL for single-null discharges [18]. Assuming a comparable turbulence intensity in DIII-D ($\delta n_g/n = 0.05$), turbulence-induced refraction of HFS-launched LH waves is expected to result in a slightly broadened off-axis current profile and negligible change in OACD ($< 1\%$ change in I_{LH} compared to the no turbulence case).This is to be compared to the C-Mod multi-pass case in Figure 6b, where turbulence at $\delta n_g/n = 0.05$ results in a significant decrease in current driven at $\rho \approx 0.65$, and a $\sim 7\%$ increase in I_{LH} compared to the no turbulence case. In C-Mod, this

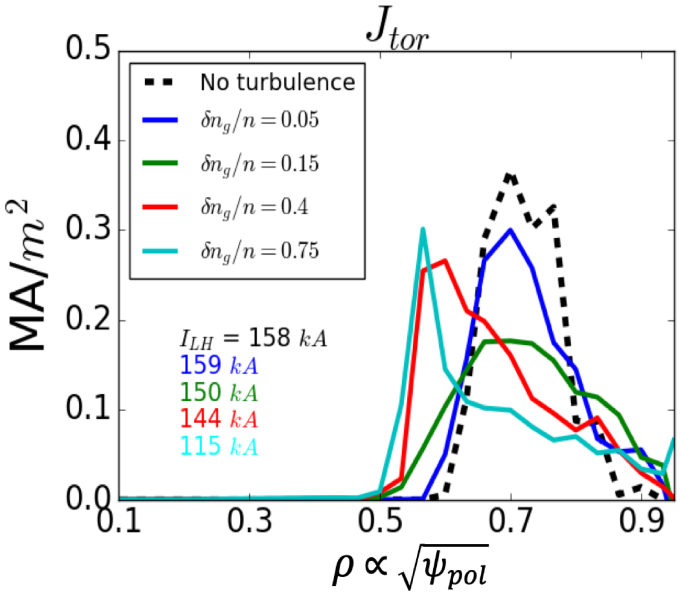

Figure 14: Predicted LHCD profile in DIII-D for HFS launch with quiescent SOL (dashed black line) and turbulent SOL (colored lines). $N_{||} = -2.7$, $P_{LH} = 1.6$ MW. $\langle FWHM \rangle = 1.5$ cm, $f_p = 0.25$. I_{LH} calculated for $\rho < 0.95$. ρ is normalized square-root of poloidal flux.

increased sensitivity of current drive performance to turbulence induced refraction is attributed to the increased stochasticity of rays in the multi-pass regime.

8 Summary and Discussion

A synthetic SOL turbulence model has been implemented in the RTFP codes GENRAY/CQL3D to study the effect of turbulence-induced refraction on LHCD. This model captures the highly structured, intermittent nature of blob-like turbulence, and how this may affect wave refraction. Steady-state current drive is calculated in a time-dependent manner to account for rapid ray-trajectory perturbation due to SOL turbulence. These results show, *a posteriori*, that the ergodic hypothesis is valid for calculating current drive, at least in a low-density C-Mod scenario.

Blob-like SOL turbulence is shown to significantly change the power deposition and current drive profile in the core. Turbulence-induced refraction is responsible for driving larger on-axis current, and mitigating off-axis peaks. Correspondingly, the resulting HXR profiles do not exhibit the unphysical "shoulder" structures predicted from standard RTFP treatment. Turbulence intensity ($\delta n_g/n$) and spatial scale ($\langle$FWHM$\rangle$) significantly affect the resulting current profile. Increasing $\delta n_g/n$ and/or decreasing $\langle$FWHM$\rangle$ leads to greater on-axis current and smoother profiles. Effects due to varying the packing fraction of blobs (f_p) are negligible. This is likely due to the gap between the grill and the separatrix being small ($\sim$1 cm). f_p may be important in reactor-relevant geometries where this gap is much larger. Nonetheless, in the thin C-Mod SOL, the free tuning of f_p allows increasing of $\delta n_g/n$ and decrease of $\langle$FWHM$\rangle$ in the blob-model while still satisfying the WKB condition for validity derived in Appendix A.

An $N_{||}$-tail is introduced to the launch spectrum to crudely account for modifications to the main lobe due to PDI. A synergy exists between the turbulence and the $N_{||}$-tail: refraction in the SOL rotates some of the high-$N_{||}$ rays into the core, allowing for more single-pass damping

near-axis. This results in more current drive on-axis than is possible with just the $N_{||}$-tail or just the SOL turbulence (Fig. 15a). The HXR profile also better matches experiment when both effects are present (Fig. 15b). Note that only $P_{tail}/P_{tot} = 0.1$ is required to match the experimental HXR shape, as opposed to the previously reported $P_{tail}/P_{tot} = 0.5$ with no turbulence [37].

Robustness of calculated steady-state profiles is greatly improved with the addition of SOL turbulence. J_{tor} profiles remained self-similar when the background density is scaled $\pm 10\%$. The rotation of $k_\perp$ due to turbulence-induced refraction acts to result in similar phase-space trajectories for rays despite changes in the background profiles. The turbulence model, or any reduced model that broadens the $k_\perp$ spectrum at launch, will be critical for robust RTFP modeling in the multi-pass regime.

In a DIII-D HFS LH launch scenario, blob-like turbulence in the SOL is expected to slightly broaden the off-axis current peak. This assumes that HFS turbulence intensity in DIII-D is comparable to measurements in Alcator C-Mod. If HFS turbulence intensity is high ($\delta n_g/n \approx 0.5$), the current profile will be significantly broadened and shifted slightly inward ($\Delta\rho_{peak} \approx -0.15$), and OACD will significantly decrease ($> 10\%$). To mitigate these effects caused by turbulence-induced refraction, either turbulence intensity, or the width of the turbulent layer, must be decreased. Both can be achieved by operating at higher I_p [50]. At expected turbulence levels ($\delta n_g/n < 0.15$), DIII-D HFS current drive performance seems insensitive to turbulence induced refraction. This is attributed to operating in the single-pass regime, where rays are less stochastic.

There seem to be two approaches to mitigating the effect of turbulence on core ELD. The first is to directly lessen the RF-turbulence scattering. This can be accomplished by operating at higher current, as described earlier. The second method is to decrease the stochasticity of the rays. This can be accomplished by operating at high core T_e (assuming the rays can access the core), as demonstrated in the DIII-D HFS simulations.

Turbulence induced refraction is shown to partially bridge the spectral-gap in C-Mod. Another important mechanism for bridging the spectral-gap is poloidal mode-number ($k_\theta r$) variation caused by the $B \propto 1/R$ dependence in a toroidal geometry [8]. For example, in C-Mod, where $\epsilon \equiv a/R \approx 0.32$, variation of the poloidal mode-number (and a subsequent $N_{||}$ upshift) allows on-axis ELD following multiple passes. This toroidal effect is weaker in smaller ϵ devices. In EAST ($\epsilon \approx 0.24$), toroidicity is insufficient to explain on-axis LH damping, even though on-axis current drive is detected in experiment [37, 51]. In this geometry, additional *toroidal* mode-number variation caused by turbulent wave-scattering may be uniquely responsible for on-axis damping. Therefore, turbulence induced refraction is expected to play a greater role in explaining the spectral-gap in low ϵ devices, like EAST and WEST ($\epsilon = 0.2$).

Lastly, even with both the SOL turbulence and inclusion of an $N_{||}$-tail model, near-axis J_{tor} is still under-predicted in C-Mod. Two possible reasons exist. First, its possible that collisional loss of LH power in the SOL is over-predicted. Second, full-wave effects in the turbulent SOL may be important. Approximately 20% of launched power is lost to collision in the SOL. Modeling a more accurate SOL and divertor geometry, ex. using the two-point model to generate background n, T profiles, may lead to less collisional loss and higher I_{LH}. However, the validity of the WKB approximation is questionable near the divertor, where there are large density gradients near the field lines separating the private flux region. The WKB approximation is also invalid in the far-SOL near the ray turning point. Lastly, its expected that blob-like turbulence in the SOL will

result in significant diffraction and partial-reflection of LH waves [27,28]. All these effects motivate the need to implement the blob-turbulence model in a full-wave edge-solver like Petra-M [52].

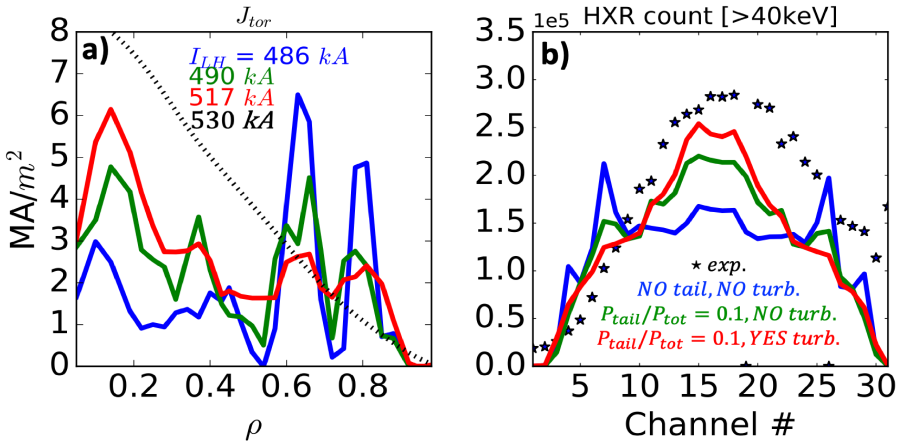

Figure 15: Modeling both SOL turbulence and $N_{||}$ tail with $P_{tail}/P_{tot} = 0.1$. GENRAY/CQL3D profiles for a) J_{tor} and b) HXR profile. Experimental J_{tor} in dashed line. Experimental HXR profile in black stars.

9 Acknowledgements

BB would like to thank Abhay Ram (MIT) for insightful discussions on RF-scattering physics, and Stephen Wukitch (MIT) for help obtaining DIII-D data. This work was supported by US DoE under contract numbers: DE-SC0018090 supporting the RF-SciDAC 4 project, DE-SC0014264 supporting PSFC MFE projects, and DE-FC02-04ER54698 supporting DIII-D projects. The simulations presented in this paper were performed on the MIT-PSFC partition of the Engaging cluster at the MGHPCC facility (www.mghpcc.org) which was funded by DoE grant number DE-FG02-91-ER54109.

10 Disclaimer

This report was prepared as an account of work sponsored by an agency of the United States Government. Neither the United States Government nor any agency thereof, nor any of their employees, makes any warranty, express or implied, or assumes any legal liability or responsibility for the accuracy, completeness, or usefulness of any information, apparatus, product, or process disclosed, or represents that its use would not infringe privately owned rights. Reference herein to any specific commercial product, process, or service by trade name, trademark, manufacturer, or otherwise, does not necessarily constitute or imply its endorse ment, recommendation, or favoring by the United States Government or any agency thereof. The views and opinions of authors expressed herein do not necessarily state or reflect those of the United States Government or any agency thereof.

Appendices

A WKB validity of blob model

The ray-tracing treatment is valid as long as the Wentzel–Kramers–Brillouin (WKB) approximation is also valid. Heuristically, this means the plasma must be homogeneous in comparison to the LH wavelength, such that

$$k_\perp L \gg 1 \tag{A.1}$$

where $L \equiv (|\frac{\nabla n}{n}|)^{-1}$. One can rigorously derive this condition for the 3D anisotropic LH wave and find that is it quite a bit more restrictive. First, the wave electric field is assumed to be of the form

$$\delta\mathbf{E} = \tilde{\mathbf{E}}(\mathbf{r})exp(i\mathbf{k}\cdot\mathbf{r} - i\omega t) \tag{A.2}$$

where $\tilde{\mathbf{E}}$ is the slowly varying amplitude. It can then be shown that

$$\boldsymbol{\nabla}\mathbf{E} = i\boldsymbol{\nabla}S\tilde{\mathbf{E}} + \boldsymbol{\nabla}\tilde{\mathbf{E}} \tag{A.3}$$

where S is the eikonal function and $\boldsymbol{\nabla}S = \mathbf{k}$. Substituting $i\boldsymbol{\nabla}S + \boldsymbol{\nabla}$ for $i\mathbf{k}$ into the Fourier transformed wave equation yields

$$\frac{c^2}{\omega^2}(\mathbf{k} - i\boldsymbol{\nabla}) \times [(\mathbf{k} - i\boldsymbol{\nabla}) \times \tilde{\mathbf{E}}] + \epsilon\cdot\tilde{\mathbf{E}} = \mathbf{D}\cdot\tilde{\mathbf{E}} = 0 \tag{A.4}$$

where ϵ is now the dielectric tensor. If $\frac{|\boldsymbol{\nabla}\tilde{\mathbf{E}}|}{|\tilde{\mathbf{E}}|} \ll \mathbf{k}$, we can neglect the $i\boldsymbol{\nabla}$ terms and arrive at the standard dispersion relation

$$\mathbf{N}\times(\mathbf{N}\times\mathbf{E}) + \epsilon\cdot\mathbf{E} = \mathbf{D_0}\cdot\tilde{\mathbf{E}} = 0 \tag{A.5}$$

where $\mathbf{N} = c\mathbf{k}/\omega$ is the refractive index. In neglecting the gradient-terms, the WKB approximation ($\mathbf{D} \approx \mathbf{D_0}$) is made. To check whether this approximation is valid, Eq. (A.4) can be expanded into terms that are zeroth and first-order in $\boldsymbol{\nabla}n$-terms. The WKB approximation requires that the first-order terms are negligible. Correspondingly, this requires:

$$\left|\frac{N_\perp^2}{N^2 - \epsilon_\perp}\epsilon_{xy} + i\frac{N_{||}^2 N_\perp^2}{(N_\perp^2 - \epsilon_{||})^2}(\epsilon_{||} - 1)\right|\frac{1}{k_\perp L} \ll 1 \tag{A.6}$$

where $\epsilon_\perp = 1 - \omega_{pi}^2/\omega^2 + \omega_{pe}^2/\omega_{ce}^2$, $\epsilon_{||} = 1 - \omega_{pi}^2/\omega^2 - \omega_{pe}^2/\omega^2$, and $\epsilon_{xy} = \omega_{pe}^2/(\omega\omega_{ce})$. The approximation $\boldsymbol{\nabla}n_{||} \approx 0$ is used. As the wave approaches a cutoff, $\epsilon_{xy}, |\epsilon_{||}| \ll 1$, and the second term in the LHS is dominant. In this limit, Eq. (A.6) reduces to:

$$\left(\frac{N_{||}}{N_\perp}\right)^2 \frac{1}{k_\perp L} \ll 1 \tag{A.7}$$

Physically, this means there is a coupling between the parallel and perpendicular electric fields that can give rise to large gradient-terms (since $N_\perp$ is small near the cut-off). While Eq. (A.7) is slightly more restrictive than Eq. (A.1), they both reveal that ray-tracing is invalid near the cut-off. Next, consider a case near the seperatrix where density is high enough such that $\epsilon_{xy} \gg 1, N^2 \approx N_\perp^2 \gg |\epsilon_{||}|$. In this limit, the first term in Eq. (A.6) is dominant. The expression reduces to

$$\epsilon_{xy}\frac{1}{k_\perp L} \ll 1 \tag{A.8}$$

The condition for WKB validity in Eq. (A.8) is significantly more restrictive than the heuristic condition in Eq. (8). This is due to a coupling between the two perpendicular components of the electric field that give rise to large gradient-terms in Eq. (A.4).

In the blob turbulence model:

$$L^{-1} = \left| \frac{\boldsymbol{\nabla} n}{n} \right| \approx 4ln(2) f_p^{-1} \langle |\Delta n| \rangle \langle \text{FWHM} \rangle^{-1}. \tag{A.9}$$

where the term $4ln(2)f_p^{-1}$ accounts for the increase in individual blob density as packing fraction decreases, but $\langle |\Delta n| \rangle$ is kept fixed. Figure 16 shows contours of the WKB validity limit (when Eq. 13 is an equality), as a function of blob-like turbulence parameters for B=4T (typical field in Alcator C-Mod LFS SOL). Solid lines correspond to $f_p = 0.2$. Dashed lines correspond to $f_p = 0.6$. The blob model is only valid to the left of these contour lines. It is evident that turbulence with $\langle |\Delta n| \rangle \approx 1$ can be validly modeled as long as care is taken to choose appropriate blob size and packing fraction. The y-axis range is bound by experimentally relevant blob sizes, $\langle \text{FWHM} \rangle = 0.5 - 5\text{cm}$.

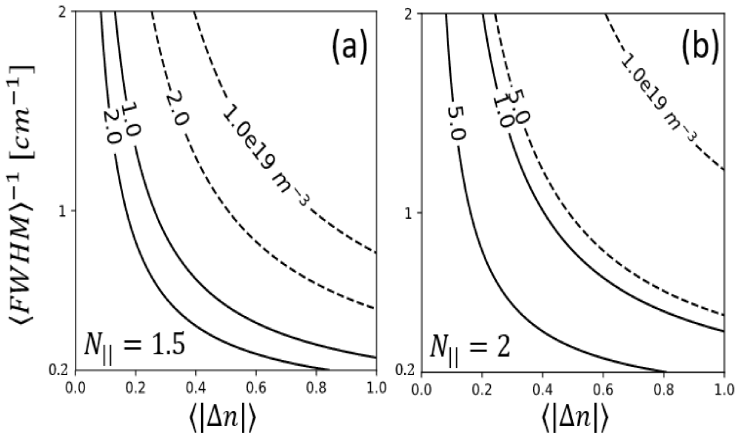

Figure 16: Contours of WKB validity limit for (a) $N_{||} = 1.5$ and (b) $N_{||} = 2$. Contour labels correspond to background n_e, with solid lines for $f_p = 0.2$ and dashed lines for $f_p = 0.6$. Ray-tracing valid left of contours. B=4T. The x-axis is the spatially averaged absolute value of density fluctuation Δn, as defined in Eq. (6). The y-axis is the inverse of the average blob width (FWHM of blob density in poloidal plane).

B Comparison to k-scattering model

The three-wave interaction treatment of wave-scattering [8,35], here called the k-scattering model, assumes a turbulent density wave-spectrum, $S(\zeta)$, of the form:

$$S(\zeta) = \frac{1}{\pi \zeta_0^2} \langle |\Delta n| \rangle^2 e^{-(\frac{\zeta}{\zeta_0})^2} \tag{B.1}$$

where ζ is the perpendicular wavenumber of the turbulence. This is a Gaussian spectrum, whose spectral width is set by ζ_0. $S(\zeta)$ is normalized such that $\int_0^\infty 2\pi\zeta S(\zeta) d\zeta = \langle |\Delta n| \rangle^2$.

The k-scattering model [8] can be directly compared to the blob-turbulence model by creating synthetic blob profiles that, when Fourier analyzed, match the spectral form of Eq. (B.1). Figure 17 shows the wave-spectrum of blob-like turbulence in the poloidal plane. Each colored line is a

spectrum calculated from a different cut on the poloidal plane. For each blob-field, 40 of these cuts are Fourier analyzed and fit to the form in Eq. (B.1) by varying ζ_0.
Interestingly, the fitted-ζ_0 of a blob-like field is sensitive to $\langle \text{FWHM} \rangle$ but robust to f_p. $S(\zeta)$ of the blob-like turbulence can be split into 2 zones: (1) the sub-blob scale ($\zeta > \langle \text{FWHM} \rangle^{-1}$) and (2) the many-blob scale ($\zeta < \langle \text{FWHM} \rangle^{-1}$). At the sub-blob scale, the shape of the wave-spectrum is dominantly affected by the wave-spectrum of individual blobs. Each blob is Gaussian in the poloidal spatial plane, and therefore perfectly fits a Gaussian when Fourier analyzed. Therefore, the best-fit ζ_0 is strongly affected by blob size, such that ζ_0 approximately scales inversely with $\langle \text{FWHM} \rangle$ (compare Fig. 17b and 17c). This scaling is only approximate because the wave-spectrum at the many-blob scale, which is not Gaussian, is simultaneously being fitted. In addition, because the wave-spectrum at the many-blob scale is not Guassian, the best-fit ζ_0 is relatively insensitive to turbulence parameters that affect this zone of the wave-spectrum (ie. f_p) (compare Fig. 17a and 17b). Therefore, blob fields of varying intermittency (set by f_p), result in wave-spectra with roughly equal ζ_0. In this sense, the blob-model accounts for an additional turbulence parameter, f_p, that the k-scattering treatment cannot capture.

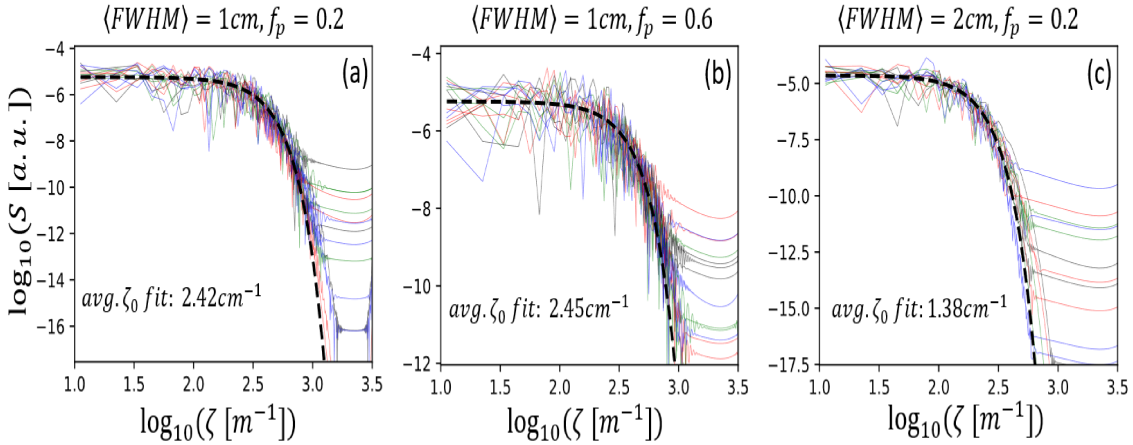

Figure 17: Spectral density of blob fields (colored lines) fit to analytic form in eq. 17 (black dashed line).

Note that while the k-scattering treatment uses a Gaussian $S(\zeta)$ for convenient analysis, a more realistic wave spectrum could, in principle, be used. The scattering kernel, which computes l_s, would require a numerical integration. However, the crucial limitation of the k-scattering treatment is the required use of the random-phase approximation (RPA). Not only does the RPA treat the turbulence as non-intermittent, it also sets statistical limits on the validity of the k-scattering treatment. These are:

$$1) \text{ if } (k_\perp/\zeta_0)^2 \gg 1 \text{ then } (k_\perp/\zeta_0)^2 < \zeta_0 l_s \tag{B.2}$$

$$2) \text{ if } k_\perp \lesssim \zeta_0 \text{ then } \zeta_0 l_s > 1 \tag{B.3}$$

Figure 18 shows contours of the k-scattering validity limit (Eq. 18 and 19), as a function of ζ_0 and $\langle |\Delta n| \rangle$. Regions left of the contour lines can be validly treated using the k-scattering model. Note that the limits of the ζ_0 axis are best-fits to the $\langle \text{FWHM} \rangle^{-1}$-axis limits in Fig. 16. In this sense, Fig. 16 and 18 approximately cover the same turbulence parameter space for easy comparison. The topology of the validity contours for the blob-model and k-scattering model are quite different. For example, in the k-scattering model, the region of validity shrinks as the turbulence scale length *increases*. At $N_{||} = 2.0$ and at high edge densities $n_e > 5 \times 10^{19}$ m^{-3},

the k-scattering model is only valid for $\langle|\Delta n|\rangle \lesssim 0.15$. This criterion is even more stringent for lower $N_{||}$ and higher n_e. Therefore, the k-scattering model is highly prohibitive in studying high-$\overline{n}$ L-mode discharges in C-Mod, where edge electron density $n_e > 5 \times 10^{19}$ m^{-3}. Bertelli et al [9] previously used the k-scattering model in high-$\overline{n}$ C-Mod discharges, but only with profiles where edge density falls to below 5×10^{19} m^{-3}. This is not a limitation for the blob model, which is valid at high edge densities and $\langle|\Delta n|\rangle$, provided f_p is sufficiently high.

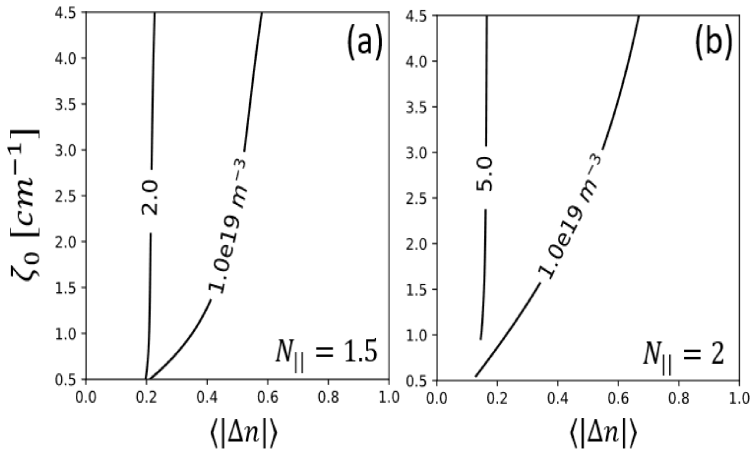

Figure 18: Contours of k-scattering model validity limit for (a) $N_{||} = 1.5$ and (b) $N_{||} = 2$. Contour labels correspond to background n_e. Model valid left of contours. B=4T. The x-axis is the spatially averaged absolute value of density fluctuation Δn, as defined in Eq. (B1). The y-axis is the turbulence wavenumber spectrum fitting term ζ_0, as defined in Eq. (B1).

C Slab result: angular diffusion of rays

A "slab-model" is created in a toroidal geometry in GENRAY in which $B_\phi \approx 5$ T, $B_{pol} = 0$, and $n_0 = 1 \times 10^{19}$ m^{-3}. Lower Hybrid rays at 4.6 GHz are launched at $N_{||} = 2$ from the mid-plane with $k_Z = 0$. In a quiescent plasma, k_Z would remain zero through the ray's trajectory. In a turbulence plasma, refraction from density fluctuations rotates the $k_\perp$ vector, resulting in a non-zero k_Z. For an ensemble of rays, this rotation is treated as a diffusion in θ-space where $\theta = tan^{-1}(k_Z/k_R)$. In the k-scattering treatment the angular diffusion coefficient $D_{\theta\theta} \propto \zeta_0 \langle|\Delta n|\rangle^2 k_\perp^{-2}$. The extent of turbulence-induced wave scattering can be quantified by this angular diffusion coefficient.

The effect of blob-intermittency on angular diffusion is studied using this slab model. Multiple rays are launched through 18 cm for blob-like turbulence with $\langle|\Delta n|\rangle = 0.15$, $\langle$FWHM$\rangle = 1$ cm and varying f_p. 2D axisymmetric blobs can be used since $B_{pol} = 0$. For the $f_p \approx 1$ case, blobs are created using a Gaussian filter method [53] to avoid overlapping blobs. For each ray, a different turbulence field is used. This is repeated for an equivalent k-scattering turbulent layer where ζ_0 is determined by the method discussed in Appendix B. Figure 19 plots a histogram of the final θ of 300 rays after traveling 18 cm in the R-direction. The histogram shape is symmetric and Gaussian, as expected from diffusion caused by turbulence that is isotropic in the perpendicular plane. Note that the standard-deviation of this Gaussian shape, σ_θ increases as f_p decreases. Therefore, turbulence-induced refraction increases with the intermittency of the blob-field. Even at $f_p \approx 1$, the extent of angular diffusion through a blob field is larger than in the k-scattering model. This is likely due to the coherent structure of the dense filaments, which leads to a qualitatively different way in which $k_\perp$ rotates. In the blob model, angular diffusion results from

large-angle rotations due to refraction from individual blobs. In contrast, the k-scattering model is dominated by frequent small-angle rotations.

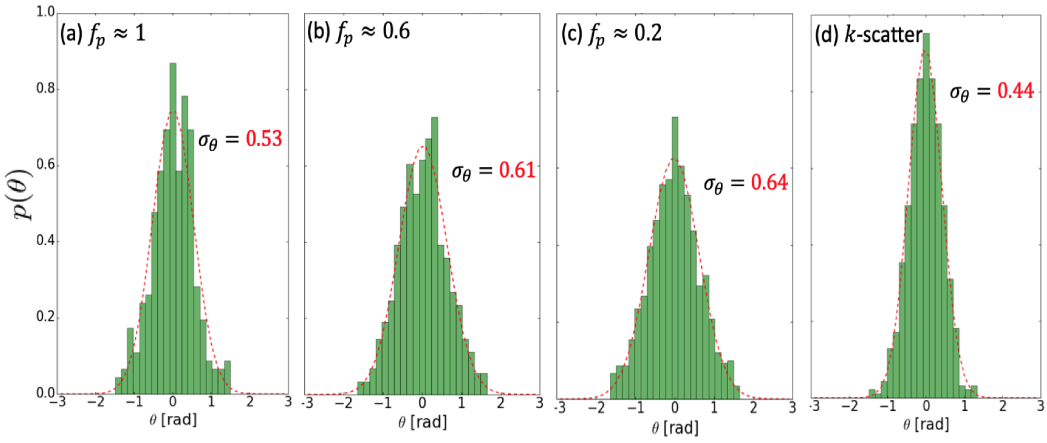

Figure 19: Slab model: Histogram of ray angular diffusion after 18cm propagating through blob-like turbulence with (a) $f_p \approx 1$, (b) $f_p = 0.6$, (c) $f_p = 0.2$, and (d) equivalent k-scattering turbulence. $\langle|\Delta n|\rangle = 0.15, \langle FWHM\rangle = 1cm$, $n_{e_0} = 1 \times 10^{19} m^{-3}, B_0 \approx 5T$. Red dashed line is Gaussian fit.

References

[1] Jardin S, Kessel C, Mau T, Miller R, Najmabadi F, Chan V, Chu M, LaHaye R, Lao L, Petrie T *et al.* 2006 *Fusion Engineering and Design* **80** 25–62

[2] Mailloux J, Alper B, Baranov Y, Becoulet A, Cardinali A, Castaldo C, Cesario R, Conway G, Challis C, Crisanti F *et al.* 2002 *Physics of Plasmas* **9** 2156–2164

[3] Reiman A and Fisch N J 2018 *Physical Review Letters* **121** 225001

[4] Bonoli P 1984 *IEEE transactions on plasma science* **12** 95–107

[5] Wallace G, Parker R, Bonoli P, Hubbard A, Hughes J, LaBombard B, Meneghini O, Schmidt A, Shiraiwa S, Whyte D *et al.* 2010 *Physics of Plasmas* **17** 082508

[6] Shiraiwa S, Baek S, Faust I, Wallace G, Bonoli P, Meneghini O, Mumgaard R, Parker R, Scott S, Harvey R *et al.* 2015 Impact of sol plasma profiles on lower hybrid current drive: Experimental evidence, mitigation and modeling approaches *AIP Conference Proceedings* vol 1689 (AIP Publishing LLC) p 030016

[7] Bellan P and Wong K 1978 *The Physics of Fluids* **21** 592–599

[8] Bonoli P T and Ott E 1982 *The Physics of Fluids* **25** 359–375

[9] Bertelli N, Wallace G, Bonoli P, Harvey R, Smirnov A, Baek S, Parker R, Phillips C, Valeo E, Wilson J *et al.* 2013 *Plasma Physics and Controlled Fusion* **55** 074003

[10] Peysson Y, Decker J, Morini L and Coda S 2011 *Plasma Physics and Controlled Fusion* **53** 124028

[11] Porkolab M, Bernabei S, Hooke W, Motley R and Nagashima T 1977 *Physical Review Letters* **38** 230

[12] Takase Y, Porkolab M, Schuss J, Watterson R, Fiore C, Slusher R and Surko C 1985 *The Physics of fluids* **28** 983–994

[13] Baek S, Wallace G, Bonoli P, Brunner D, Faust I, Hubbard A, Hughes J, LaBombard B, Parker R, Porkolab M *et al.* 2018 *Physical review letters* **121** 055001

[14] Mumgaard R T 2015 *Lower hybrid current drive on Alcator C-Mod: Measurements with an upgraded MSE diagnostic and comparisons to simulation* Ph.D. thesis Massachusetts Institute of Technology

[15] Peysson Y, Team T S *et al.* 2000 *Plasma Physics and Controlled Fusion* **42** B87

[16] Decker J, Peysson Y, Artaud J F, Nilsson E, Ekedahl A, Goniche M, Hillairet J and Mazon D 2014 *Physics of Plasmas* **21** 092504

[17] Wukitch S, Shiraiwa S, Wallace G, Bonoli P, Holcomb C and Pinsker R 2017 *EPJ Web of Conferences* **157** 02012

[18] Terry J, Zweben S, Hallatschek K, LaBombard B, Maqueda R, Bai B, Boswell C, Greenwald M, Kopon D, Nevins W *et al.* 2003 *Physics of Plasmas* **10** 1739–1747

[19] Smick N, LaBombard B and Pitcher C S 2005 *Journal of Nuclear Materials* **337** 281–285

[20] Durst R, Fonck R, Kim J, Paul S, Bretz N, Bush C, Chang Z and Hulse R 1993 *Physical review letters* **71** 3135

[21] Terry J, Maqueda R, Pitcher C, Zweben S, LaBombard B, Marmar E, Pigarov A Y and Wurden G 2001 *Journal of nuclear materials* **290** 757–762

[22] Andrews P and Perkins F 1983 *The Physics of Fluids* **26** 2537–2545

[23] Tynan G, Fujisawa A and McKee G 2009 *Plasma Physics and Controlled Fusion* **51** 113001

[24] Smirnov A and Harvey R 2001 *CompX Report No. CompX-2000-01*

[25] Harvey R and McCoy M 1992 The cql3d fokker-planck code *Proceedings of the IAEA Technical Committee Meeting on Simulation and Modeling of Thermonuclear Plasmas* pp 489–526

[26] Shiraiwa S, Fredian T, Hillairet J and Stillerman J 2016 *Fusion Engineering and Design* **112** 835–838

[27] Ioannidis Z C, Ram A K, Hizanidis K and Tigelis I G 2017 *Physics of Plasmas* **24** 102115

[28] Lau C, Martin E, Shiraiwa S and Wallace G 2020 *Nuclear Fusion* **60** 036001

[29] Wright J C, Bonoli P, Schmidt A, Phillips C, Valeo E, Harvey R and Brambilla M 2009 *Physics of Plasmas* **16** 072502

[30] Shiraiwa S, Ko J, Meneghini O, Parker R, Schmidt A, Scott S, Greenwald M, Hubbard A, Hughes J, Ma Y *et al.* 2011 *Physics of Plasmas* **18** 080705

[31] Meneghini O 2012 *Full-wave modeling of lower hybrid waves on Alcator C-Mod* Ph.D. thesis

[32] Graves J, Horacek J, Pitts R and Hopcraft K 2005 *Plasma Physics and Controlled Fusion* **47** L1

[33] Kirk A, Ayed N B, Counsell G, Dudson B, Eich T, Herrmann A, Koch B, Martin R, Meakins A, Saarelma S *et al.* 2006 *Plasma Physics and Controlled Fusion* **48** B433

[34] Zweben S, Stotler D, Terry J, LaBombard B, Greenwald M, Muterspaugh M, Pitcher C, Group A C M, Hallatschek K, Maqueda R *et al.* 2002 *Physics of Plasmas* **9** 1981–1989

[35] Ott E 1979 *The Physics of Fluids* **22** 1732–1736

[36] Cesario R, Cardinali A, Castaldo C, Paoletti F and Mazon D 2004 *Physical review letters* **92** 175002

[37] Peysson Y, Decker J, Nilsson E, Artaud J, Ekedahl A, Goniche M, Hillairet J, Ding B, Li M, Bonoli P *et al.* 2016 *Plasma Physics and Controlled Fusion* **58** 044008

[38] Sierchio J, Cziegler I, Terry J, White A and Zweben S 2016 *Review of Scientific Instruments* **87** 023502

[39] Andrews P and Perkins F 1983 *The Physics of fluids* **26** 2546–2557

[40] Grulke O, Terry J, Cziegler I, LaBombard B and Garcia O 2014 *Nuclear Fusion* **54** 043012

[41] Agostini M, Zweben S, Cavazzana R, Scarin P, Serianni G, Maqueda R and Stotler D 2007 *Physics of Plasmas* **14** 102305

[42] Carralero D, Artene S, Bernert M, Birkenmeier G, Faitsch M, Manz P, de Marne P, Stroth U, Wischmeier M, Wolfrum E *et al.* 2018 *Nuclear Fusion* **58** 096015

[43] Zweben S, Terry J, LaBombard B, Agostini M, Greenwald M, Grulke O, Hughes J, D'Ippolito D, Krasheninnikov S, Myra J *et al.* 2011 *Journal of nuclear materials* **415** S463–S466

[44] Shiraiwa S, Meneghini O, Parker R, Wallace G, Wilson J, Faust I, Lau C, Mumgaard R, Scott S, Wukitch S *et al.* 2011 *Nuclear Fusion* **51** 103024

[45] Liptac J, Parker R, Tang V, Peysson Y and Decker J 2006 *Review of Scientific Instruments* **77** 103504

[46] Bizarro J P and Moreau D 1993 *Physics of Fluids B: Plasma Physics* **5** 1227–1238

[47] Baek S, Parker R, Shiraiwa S, Wallace G, Bonoli P, Brunner D, Faust I, Hubbard A, LaBombard B and Porkolab M 2013 *Plasma Physics and Controlled Fusion* **55** 052001

[48] Bonoli P, Wallace G, Shiraiwa S, Baek S, Doody J, Greenwald M, LaBombard B, Leccacorvi R, Filar K, Lin Y *et al.* 2018 *Nuclear Fusion* **58** 126032

[49] Seltzman A, Shiraiwa S, Wallace G and Wukitch S 2019 *Nuclear Fusion* **59** 096003

[50] Cziegler I, Terry J, Hughes J and LaBombard B 2010 *Physics of Plasmas* **17** 056120

[51] Zhai X, Xiang N, Chen J, Bonoli P, Shiraiwa S, Garofalo A, Yang C, Li M, Qian J, Li G *et al.* 2019 *Plasma Physics and Controlled Fusion* **61** 045002

[52] Shiraiwa S, Wright J, Bonoli P, Kolev T and Stowell M 2017 *EPJ Web of Conferences* **157** 03048

[53] Klein M, Sadiki A and Janicka J 2003 *Journal of Computational Physics* **186** 652–665